PAPER

Check for updates

Exploring bioMOF-on-MOF hybrid nanostructure for controlled drug release: characterization, kinetic modeling, and *in vitro* evaluation

Luan Minh Nguyen, [iD] [ab] Giao Thuy Quynh Vu, [iD] [a] Manh Hoang Tran, [iD] [a] Thi My Huyen Nguyen, [iD] [a] Tan Phat Nguyen, [iD] [a] Qui Thanh Hoai Ta, [iD] [ab] Dieu Linh Tran [iD] [ab] and Dai Hai Nguyen [iD] ★[ab]

In recent years, metal–organic frameworks (MOFs) have attracted significant attention as versatile materials for drug delivery systems due to their customizable structural properties. Building on this trend, we report the successful development of a bioMOF-on-MOF hybrid nanostructure, denoted as CuGA/CUR@ZIF-8 (CGCZ), as a promising controlled drug delivery platform synthesized *via* a straightforward sonochemical synthesis approach. Based on advanced physicochemical analyses, CGCZ exhibited a hydrodynamic diameter of approximately 160 nm and a polydispersity index below 0.2, indicating its suitability for drug delivery applications. Notably, CGCZ demonstrated pH-responsive drug release with superior control compared to its precursor materials, following the Higuchi model at pH 7.4 and 6.8, and the Korsmeyer–Peppas model at pH 5.5. *In vitro* cytotoxicity assays revealed that CGCZ exhibited enhanced selective cytotoxicity toward MCF-7 cancer cells while maintaining high biocompatibility with L929 normal cells. These results suggest that CGCZ is a promising candidate for controlled drug delivery in cancer therapy, highlighting the potential of bioMOF-on-MOF hybrid systems for biomedical applications.

1. Introduction

Metal–organic frameworks (MOFs) are crystalline porous materials composed of metal ions or clusters coordinated to organic linkers. These materials offer remarkable tunability in composition, pore size, and surface functionality.[1,2] Over the past decade, MOFs have garnered increasing attention in the biomedical field, particularly in applications such as biosensing, imaging, and drug delivery, owing to their controllable architectures and ability to release therapeutic agents in a precise manner.[3–5] Several MOF families have demonstrated promising drug delivery capabilities both *in vitro* and *in vivo*, including the zeolitic imidazolate frameworks (*e.g.*, ZIF-8, ZIF-90, ZIF-67),[2,6,7] the Materials of Institute Lavoisier (*e.g.*, MIL-100, MIL-101, MIL-53, MIL-125),[7–9] and the biological MOFs (*e.g.*, metal-gallate, metal-curcumin, metal-cyclodextrin).[10–13] Notably, the clinical potential of MOFs is becoming increasingly tangible. In 2023, a MOF named RiMO-301, which is constructed from hafnium ions and porphyrin ligands, became the first MOF-based nanoplatform to enter human clinical trials as a radiosensitizer.[14,15]

In addition to their use as individual components, MOFs can also be integrated to form MOF-on-MOF architectures, which offer several advantageous properties for biomedical applications. For instance, Zhong *et al.*[16] successfully developed a ZIF-8/MIL-100(Fe) hybrid structure exhibiting a remarkably high tetracycline adsorption capacity of up to 1288 mg g^{-1}. In another study, Yang *et al.*[17] constructed a GaMOF/TiMOF hybrid for ultrasound-assisted cancer therapy. This system demonstrated a tumor inhibition rate of 96.1% in 4T1 tumor-bearing mice, which was 2.9 times higher than that achieved using TiMOF alone. In a different approach, Dong *et al.*[18] coated ZIF-8 onto the surface of PCN-224 loaded with the growth factor dimethyloxalylglycine. The ZIF-8 shell acted as a regulatory barrier, enabling pH-responsive release of dimethyloxalylglycine, with 72% released at pH 5.5 compared to 48.1% at pH 7.4. Similarly, Ni's group[19] designed a MOF-on-MOF system by coating NH_2-MIL-88B onto doxorubicin-loaded NH_2-MIL-88B. This hybrid nanostructure not only exhibited pH-responsive doxorubicin release but also responded to glutathione, thereby enhancing its anticancer efficacy. Nevertheless, despite these promising advancements, MOF-on-MOF systems still suffer from several inherent drawbacks, including: (i) prolonged reaction

[a] *Institute of Advanced Technology, Vietnam Academy of Science and Technology, 1B TL29 Street, An Phu Dong Ward, Ho Chi Minh City 700000, Vietnam. E-mail: nguyendaihai@iat.vast.vn, nguyendaihai0511@gmail.com*

[b] *Graduate University of Science and Technology, Vietnam Academy of Science and Technology, 18 Hoang Quoc Viet Street, Nghia Do Ward, Hanoi 100000, Vietnam*

times, (ii) the requirement for elevated synthesis temperatures, and (iii) the reliance on hazardous reagents such as dimethylformamide and hydrochloric acid.[16–19]

Inspired by these advancements and challenges, we developed a novel bioMOF-on-MOF hybrid nanostructure for controlled drug delivery that directly addresses the inherent drawbacks of conventional MOF-on-MOF systems. In this system, ZIF-8 (Z) was selected as the core MOF due to its high drug loading capacity, pH-responsive release properties, and low cytotoxicity.[2,6,20] Curcumin (CUR), a model hydrophobic drug, was directly incorporated into the Z framework during synthesis to form CUR@ZIF-8 (CZ), thereby eliminating the need for a post-loading step and shortening the processing time. The CZ core was subsequently coated with copper-gallate (CuGA) bioMOF to yield CuGA/CUR@ZIF-8 (CGCZ). This CuGA shell functions as a gatekeeper, regulating drug release and enhancing structural stability. Additionally, the presence of gallic acid, derived from CuGA, may further contribute to therapeutic outcomes through its known antioxidant, anti-inflammatory, and anticancer activities.[21–23] To overcome the limitations of previous MOF-on-MOF strategies, green chemistry principles were integrated into the fabrication of CGCZ hybrid nanoparticles. A rapid sonochemical synthesis method was employed to significantly shorten the reaction time, while the process was conducted at room temperature without additional heating, using water as the primary solvent to avoid hazardous organic reagents. These features ensure both efficiency and sustainability while maintaining successful MOF crystallization.

Besides, the physicochemical properties of the CGCZ hybrid nanoparticles were thoroughly characterized using dynamic light scattering (DLS), zeta potential analysis, Fourier-transform infrared spectroscopy (FT-IR), X-ray diffraction (XRD), thermogravimetric analysis (TGA), field emission scanning electron microscopy (FESEM), and energy-dispersive X-ray spectroscopy (EDX). The pH-responsive release profile was investigated under physiologically relevant conditions at pH 7.4, 6.8, and 5.5. Drug release kinetics were analyzed using several mathematical models, including zero-order, first-order, Hixson–Crowell, Higuchi, and Korsmeyer–Peppas models. *In vitro* cytotoxicity assessments were conducted on both normal and cancerous cell lines to evaluate the biosafety and therapeutic efficacy of the CGCZ hybrid nanoparticles.

2. Experimental section

2.1. Synthesis of Z

The Z was synthesized *via* a sonochemical synthesis method as follows: 300 mg of zinc nitrate hexahydrate (Zn^{2+}) was dissolved in 10 mL of deionized water (DI) (solution 1), and 660 mg of 2-methylimidazole (2-MIM) was dissolved in 20 mL of methanol (solution 2). Solution 1 was added to solution 2, and the mixture was sonicated for 5 min to form Z. The product was collected by centrifugation (15 000 rpm, 10 min), freeze-dried for 24 h, and stored at 8 °C.

2.2. Synthesis of CZ

The CZ was synthesized *via* a sonochemical method similar to that used for Z, except that 10 mg of CUR was added to solution 2 prior to sonication.

2.3. Synthesis of CGCZ

The CGCZ was synthesized by dispersing 100 mg of CZ in 5 mL of DI (solution 1). Separately, 62.3 mg of gallic acid monohydrate (GA) and 20 mg of copper(II) nitrate trihydrate (Cu^{2+}) were dissolved in 30 mL (solution 2) and 5 mL (solution 3) of DI, respectively. Solutions 1 and 3 were sequentially added to solution 2, followed by sonication for 5 min to form CGCZ. The product was collected by centrifugation, freeze-dried, and stored as described above.

2.4. Drug loading and encapsulation efficiency

The drug encapsulation efficiency (EE) and loading capacity (LC) of CZ and CGCZ were quantitatively evaluated following the complete acidic degradation of the samples. Specifically, 5 mg of the dried CZ or CGCZ was dispersed in 50 μL of HCl 1 M to ensure thorough decomposition of the framework, followed by vigorous agitation for 2–3 min. The resulting suspension was then diluted to 2 mL with DI and filtered through a 0.45 μm membrane to eliminate any insoluble residues. The amount of CUR loaded was analyzed by measuring the absorbance at a fixed wavelength of 425 nm using a UV-vis light. The CUR concentration was determined based on a pre-established standard calibration curve, and the EE and LC values were subsequently calculated using standard formulas.

$$EE = \frac{m_{loaded\ drug}}{m_{added\ drug}}$$

$$LC = \frac{m_{loaded\ drug}}{m_{drug\text{-}loaded\ nanoparticles}}$$

where: $m_{loaded\ drug}$ is the total amount of CUR loaded into the structure. $m_{added\ drug}$ is the initial amount of drug added. $m_{drug\text{-}loaded\ nanoparticles}$ is the total amount of drug-loaded nanoparticles used for the decomposition.

2.5. Drug release at different pH values

The pH-responsive drug release profile of CZ and CGCZ was systematically investigated under physiologically relevant conditions to assess their release behavior in environments mimicking normal and tumor tissues. For this purpose, 30 mg of each sample was enclosed in a dialysis membrane (MWCO = 3.5 kDa) and immersed in phosphate-buffered saline (PBS) medium of varying pH values (pH 7.4, 6.8, and 5.5), representing physiological, mildly acidic, and tumor microenvironments, respectively, and maintained at 37 °C. At predetermined time intervals, 1 mL of the external release medium was collected and replaced with an equal volume of fresh buffer to maintain sink conditions and ensure sustained diffusion. The amount of CUR released into the medium was quantified by measuring the absorbance at a fixed wavelength of 425 nm

using a UV-vis. The drug release percentage was calculated using the following equation:

$$\text{Drug release percentage } (\%) = \frac{W_t}{W_i}$$

where: W_t represents the cumulative amount of drug released at time t. W_i represents the total amount of drug initially loaded within the material.

2.6. Drug release kinetic modeling

To elucidate the underlying release mechanisms, the experimental drug release data were fitted to a series of established kinetic models, including zero-order, first-order, Hixson–Crowell, Higuchi, and Korsmeyer–Peppas models. These models enable a systematic and quantitative assessment of the release kinetics, providing insights into the diffusion, dissolution, and matrix erosion processes governing drug release from the materials. The detailed equations are provided in the SI.

2.7. *In vitro* cytotoxicity evaluation

The cytotoxic effects of Z, CZ, and CGCZ materials were systematically assessed using the MTT assay on two representative cell lines: mouse fibroblasts (L929) to evaluate biocompatibility, and human breast cancer cells (MCF-7) to investigate anticancer potential. Both cell lines were cultured under standard conditions in Dulbecco's modified Eagle medium supplemented with 10% fetal bovine serum and 1% penicillin–streptomycin. Cells were maintained in a humidified incubator at 37 °C with 5% CO_2 to ensure optimal growth and viability throughout the experimental procedures. For the assay, 90 μL of cell suspension was seeded into 96-well plates at a density of 1×10^4 cells per well and incubated overnight to allow for cell adhesion. Subsequently, 10 μL of the test materials at varying concentrations (12.5, 25, 50, 100, and 200 μg mL^{-1}) were added to each well, and the plates were incubated for an additional 24 h under standard culture conditions. After treatment, cellular morphology was observed and captured by using the microscope. The medium was then removed, and cells were
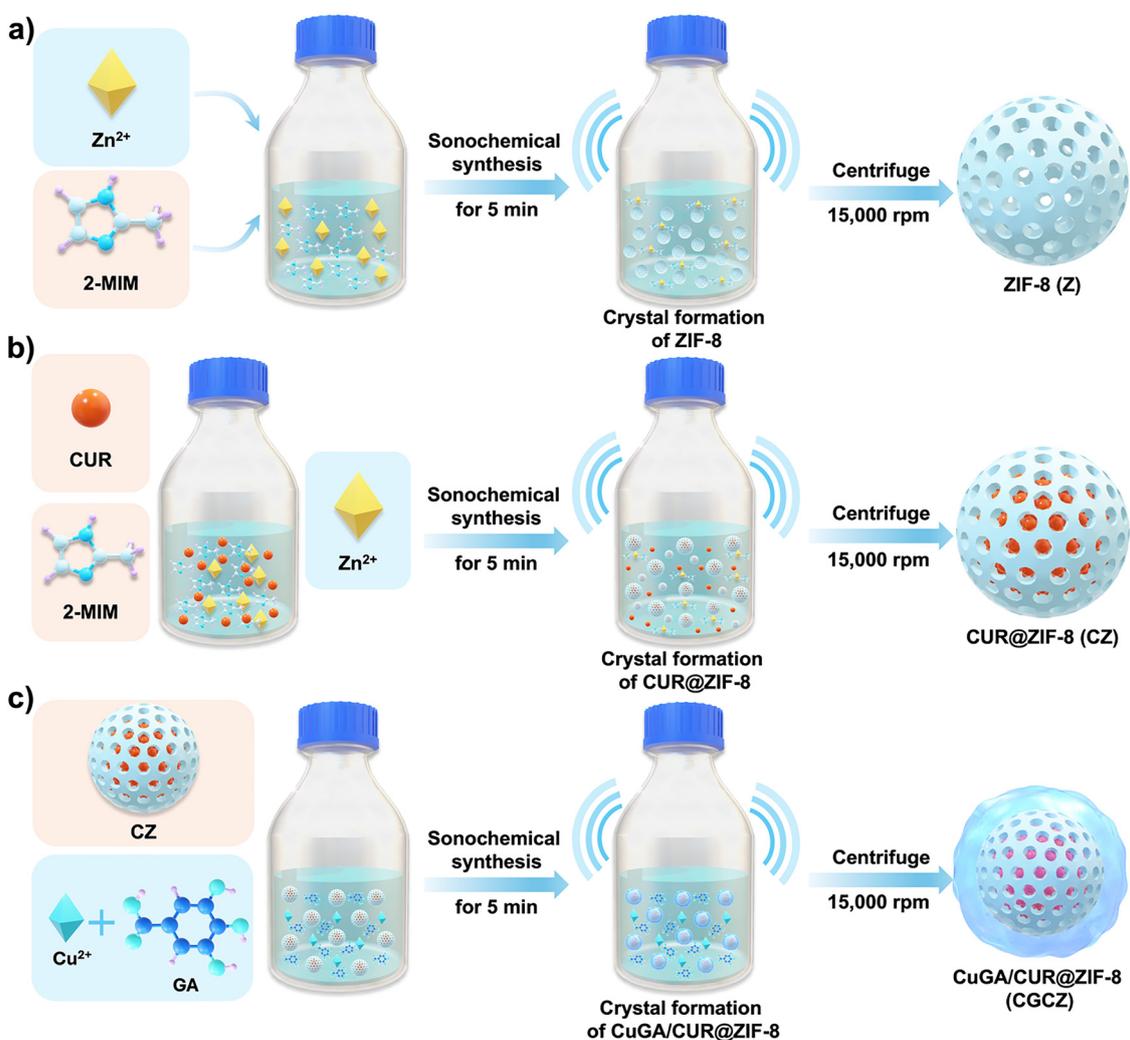

Fig. 1 Schematic representation of the sonochemical synthesis of (a) Z, (b) CZ, and (c) CGCZ.

gently washed twice with PBS to eliminate residual materials. Next, 50 μL of 3-(4,5-dimethylthiazol-2-yl)-2,5-diphenyltetrazolium bromide (MTT) solution (0.5 mg mL^{-1}) was added to each well, followed by incubation for 4 h at 37 °C to allow for the formation of formazan crystals. The resulting formazan was dissolved by adding 100 μL of dimethyl sulfoxide to each well. The absorbance was measured at fixed wavelength of 540 nm using a microplate reader to determine cell viability. The cell viability was calculated relative to untreated controls.

$$\text{Cell viability (\%)} = \frac{\text{Abs}_{\text{sample}} - \text{Abs}_{\text{blank}}}{\text{Abs}_{\text{control}} - \text{Abs}_{\text{blank}}}$$

where: $\text{Abs}_{\text{sample}}$ is the absorbance of cells treated with the test samples. $\text{Abs}_{\text{control}}$ is the absorbance of the untreated control cells. $\text{Abs}_{\text{blank}}$ is the absorbance of the blank containing only the MTT reagent without cells.

2.8. Statistical analysis

All experimental data are presented as mean values ± standard deviation, based on triplicate measurements ($n = 3$) to ensure reproducibility and accuracy. Statistical analysis was performed using Microsoft Excel, applying a two-tailed Student's t-test assuming equal variances to assess the significance of differences between groups. Statistical significance was denoted as follows: $p < 0.05$ (*), $p < 0.01$ (**), and $p < 0.001$ (***).

3. Results and discussion

3.1. Preparation

Fig. 1a–c illustrates the synthesis of Z, CZ, and CGCZ, respectively. Initially, Z was synthesized via a sonochemical process using Zn^{2+} and 2-MIM. Ultrasonic irradiation for 5 min rapidly facilitated the formation of uniform Z nanocrystals. Subsequently, CZ was prepared by a one-pot sonochemical approach. In this procedure, the amounts of Zn^{2+} and 2-MIM were kept consistent with the Z synthesis, while CUR was introduced into the reaction mixture. The ultrasonic irradiation promoted the loading of CUR within the Z framework, resulting in a high EE of 89.35% and LC of 10.72% (Fig. 2h). Finally, CGCZ was synthesized by dispersing CZ in an aqueous solution of GA, followed by the addition of Cu^{2+}. Under ultrasonic irradiation for 5 min, an in situ self-assembly process formed the CuGA bioMOF layer on the CZ surface. The CGCZ sample exhibited an EE of 73.60% and an LC of 8.83% (Fig. 2h). The reduction in EE
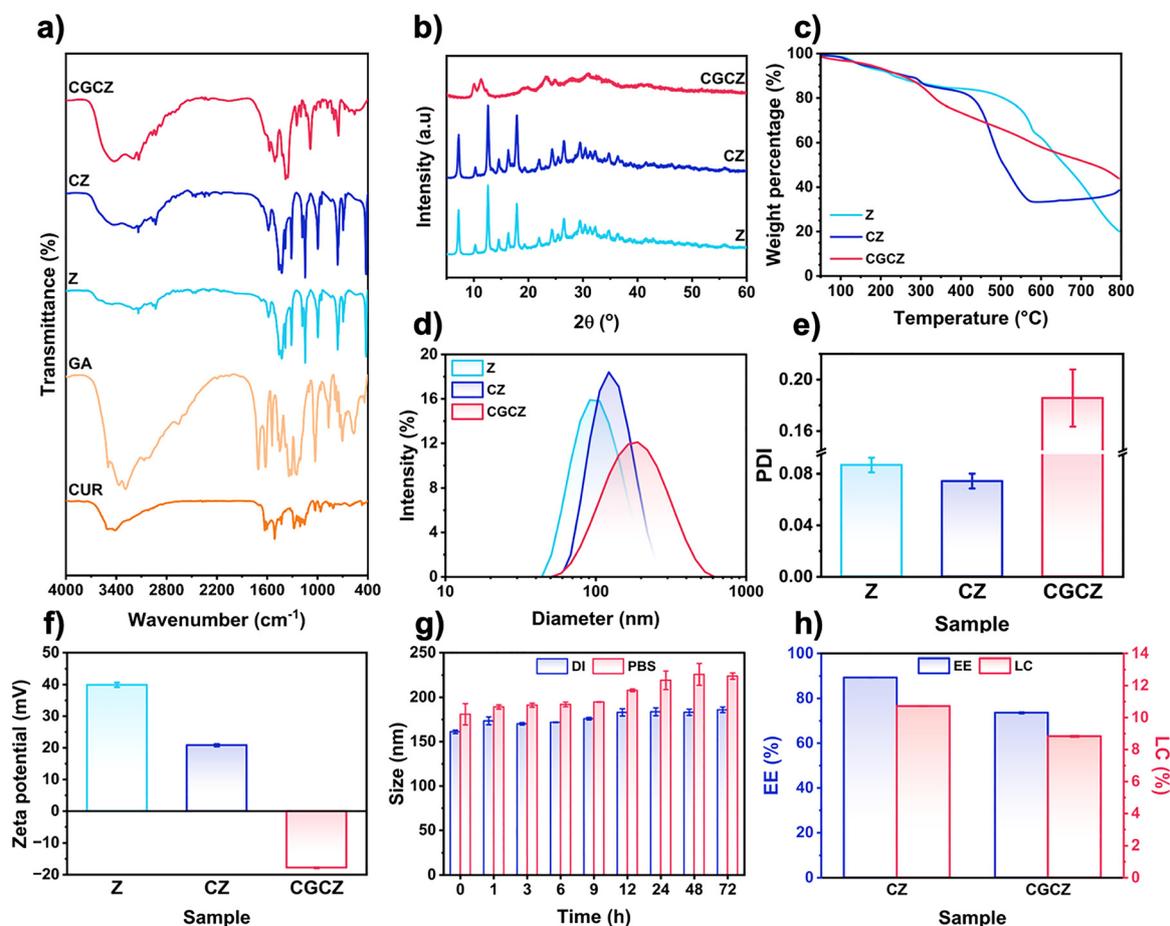

Fig. 2 (a)–(f) Characterization of Z, CZ, and CGCZ using various techniques: (a) FT-IR spectra compared with GA and CUR, (b) XRD patterns, (c) TGA profiles, (d) hydrodynamic diameter, (e) PDI by DLS, and (f) zeta potential analysis. (g) Stability of CGCZ in DI water and PBS over 72 h. (h) Evaluation of the loading profiles of CZ and CGCZ, presented as EE and LC.

and LC compared to the CZ sample could be attributed to the partial leakage or displacement of CUR during the bioMOF coating process, likely due to structural rearrangements induced by the ultrasonic treatment. Overall, this sequential sonochemical approach enabled the successful synthesis of Z, CZ, and CGCZ materials with tunable surface characteristics and high CUR loading, highlighting their potential application in drug delivery systems.

3.2. Characterization

To gain comprehensive insight into the surface chemical features of the synthesized materials, FT-IR spectra of CGCZ, CZ, Z, GA, and CUR were analyzed. As shown in Fig. 2a, the Z sample exhibited characteristic vibrational bands, including N–H stretching (3573–3189 cm^{-1}), C–H stretching (3137 and 3042–2931 cm^{-1}), C=N stretching (1584 cm^{-1}), entire imidazole ring stretching (1459 and 1384 cm^{-1}), imidazole ring in-plane bending (1350–950 cm^{-1}), aromatic sp^2 C–H bending (760 and 693 cm^{-1}), and Zn–N stretching (422 cm^{-1}), which are consistent with previously reported features of Z.[24–26] For CUR, characteristic absorption bands were observed at 3499–3414 cm^{-1} (O–H stretching), 1627 cm^{-1} (C=C stretching), 1592 and 1502 cm^{-1} (C=C skeletal vibrations of the benzene ring), 1407 cm^{-1} (C–H bending of the hydrocarbon group), 1280–1028 cm^{-1} (C–O stretching), and 978 and 815 cm^{-1} (C–H out-of-plane rocking).[27,28] In the case of the CZ sample, the FT-IR spectrum is predominantly dominated by the characteristic peaks of Z, while the signals of CUR are less distinguishable, a phenomenon that has also been reported in previous studies.[29–31] This observation can be attributed to the strong vibrational modes of the Z framework overlapping with and masking the characteristic vibrations of CUR. Furthermore, the results also contribute to confirming that the structural integrity of the Z framework remains intact upon the incorporation of CUR. In contrast, the FT-IR spectrum of CGCZ, which was formed by coating the CZ core with a CuGA bioMOF layer, exhibited several noticeable changes, strongly indicating successful surface functionalization. Specifically, the intensity of several characteristic peaks of CZ decreased and exhibited slight shifts, most prominently at 1584, 1426, 1310, 1147, 996, 760, 694, and 422 cm^{-1}. These changes suggest interactions between the CuGA coating and the Z framework. Additionally, an enhancement in the absorption band around 3422 cm^{-1} was observed, likely associated with O–H stretching vibrations from GA in the CuGA layer.[32,33] The appearance of new bands in the range of 618–508 cm^{-1} may also be attributed to Cu–O vibrations characteristic of the CuGA structure.[34,35]

The XRD patterns shown in Fig. 2b offer additional insight into the crystalline evolution of the materials during each modification step. For the pristine Z sample, a series of sharp diffraction peaks appeared at 7.20° (011), 10.24° (002), 12.57° (112), 14.56° (022), 16.35° (013), 17.87° (222), 19.31° (123), 22.00° (114), 24.30° (233), 25.40° (224), 26.50° (134), 29.51°, 30.37° (224), 31.32° (235), 34.69° (226), and 36.44° (444). These peaks are in excellent agreement with the standard diffraction pattern of Z, confirming the successful formation of a highly

crystalline Z framework.[36,37] Upon drug loading, the CZ sample retained a diffraction profile closely resembling that of Z, albeit with minor peak shifts to 7.22, 10.28, 12.59, 14.60, 16.31, 17.91, 19.31, 22.00, 24.30, 25.50, 26.48, 29.47, 30.47, 31.28, 34.73, and 36.41°. These subtle deviations are likely attributed to the incorporation of CUR molecules into the porous framework, which may slightly distort the lattice symmetry or parameters. Nonetheless, the preserved peak positions and intensities indicate that the fundamental Z structure remains largely intact after drug loading. Meanwhile, the XRD pattern of the CGCZ sample displayed more distinct alterations, suggesting structural changes resulting from the deposition of the CuGA shell on the CZ surface. Diffraction peaks appearing at 10.10° (200), 13.16° (011), 20.01° (112), 28.03° (213), 31.09° (413), 41.84° (613), and 42.85° (132) matched well with the characteristic reflections of CuGA.[32,33,38] Additionally, several weak and broadened peaks at 10.28, 12.59, 19.31, 25.50, and 31.28° may be attributed to the underlying CZ structure being partially masked by the outer CuGA layer. These findings further confirm the successful surface functionalization of CZ with a bioMOF coating.

TGA was employed to investigate and compare the thermal stability of the materials Z, CZ, and CGCZ, with the results presented in Fig. 2c. In the temperature range of 30–110 °C, all three samples exhibited a slight mass loss of approximately 1.85%, which is generally attributed to the evaporation of physically adsorbed water molecules on the material surfaces. At around 400 °C, both Z and CZ displayed similar mass losses of approximately 15.76%, primarily due to the partial decomposition of organic components such as 2-MIM and CUR incorporated within the frameworks. This observation suggests that the incorporation of CUR into CZ does not significantly affect the thermal stability of the Z framework. Meanwhile, CGCZ showed a higher mass loss (26.56%) within this temperature range, likely due to the decomposition of the CuGA coating functionalized onto the CZ surface. This result is consistent with previous reports on the thermal behavior of this bioMOF,[39,40] further confirming the successful functionalization of the CZ surface with bioMOF. As the temperature was further increased to 800 °C, all samples experienced substantial decomposition. Specifically, Z exhibited a total mass loss of 79.92%, while CZ and CGCZ lost 61.40% and 56.08% of their masses, respectively. The residual mass can be attributed to the formation of metal oxides such as CuO, Cu$_2$O, or ZnO, which are the typical decomposition products of the metal-containing components in these materials.[39–41]

The hydrodynamic diameter and polydispersity index (PDI) of the Z, CZ, and CGCZ were characterized using DLS to evaluate the size distribution and uniformity of the materials after successive functionalization steps (Fig. 2d and e). The pristine Z exhibited an average particle size of 96.44 nm with a low PDI of 0.09, indicating a highly monodisperse system. Following the addition of CUR, the particle size of CZ increased markedly to 121.90 nm, which suggests the successful incorporation of CUR into the structure of Z. Notably, the PDI of CZ remained low at 0.07, demonstrating that the particle size

distribution remained narrow and uniform even after drug loading. Further surface functionalization with the CuGA bioMOF coating resulted in an additional increase in particle size for CGCZ, reaching 160.20 nm. This indicates the successful formation of the bioMOF shell around the CZ core. However, the PDI of CGCZ increased to 0.19, reflecting a broader size distribution compared to Z and CZ. Despite this increase, the PDI remained below 0.2, which is generally considered acceptable for biomedical applications, indicating that the overall uniformity of the system was maintained at a satisfactory level. The colloidal stability of CGCZ was further assessed

in both DI and PBS. As presented in Fig. 2g, the particle size of CGCZ showed excellent stability in DI, with a negligible change (approximately 25 nm) after 72 h of incubation. In contrast, an increase in particle size over time was observed in PBS, which may be attributed to the potential attack of phosphate anions on the coordination bonds within the CGCZ framework, leading to partial disruption.[42,43]

Fig. 2f presents the zeta potential data for the Z, CZ, and CGCZ samples. Specifically, Z exhibited a zeta potential of 39.93 mV, reflecting a strongly positively charged surface characteristic of Zn^{2+} ions on the structure of Z. In contrast,
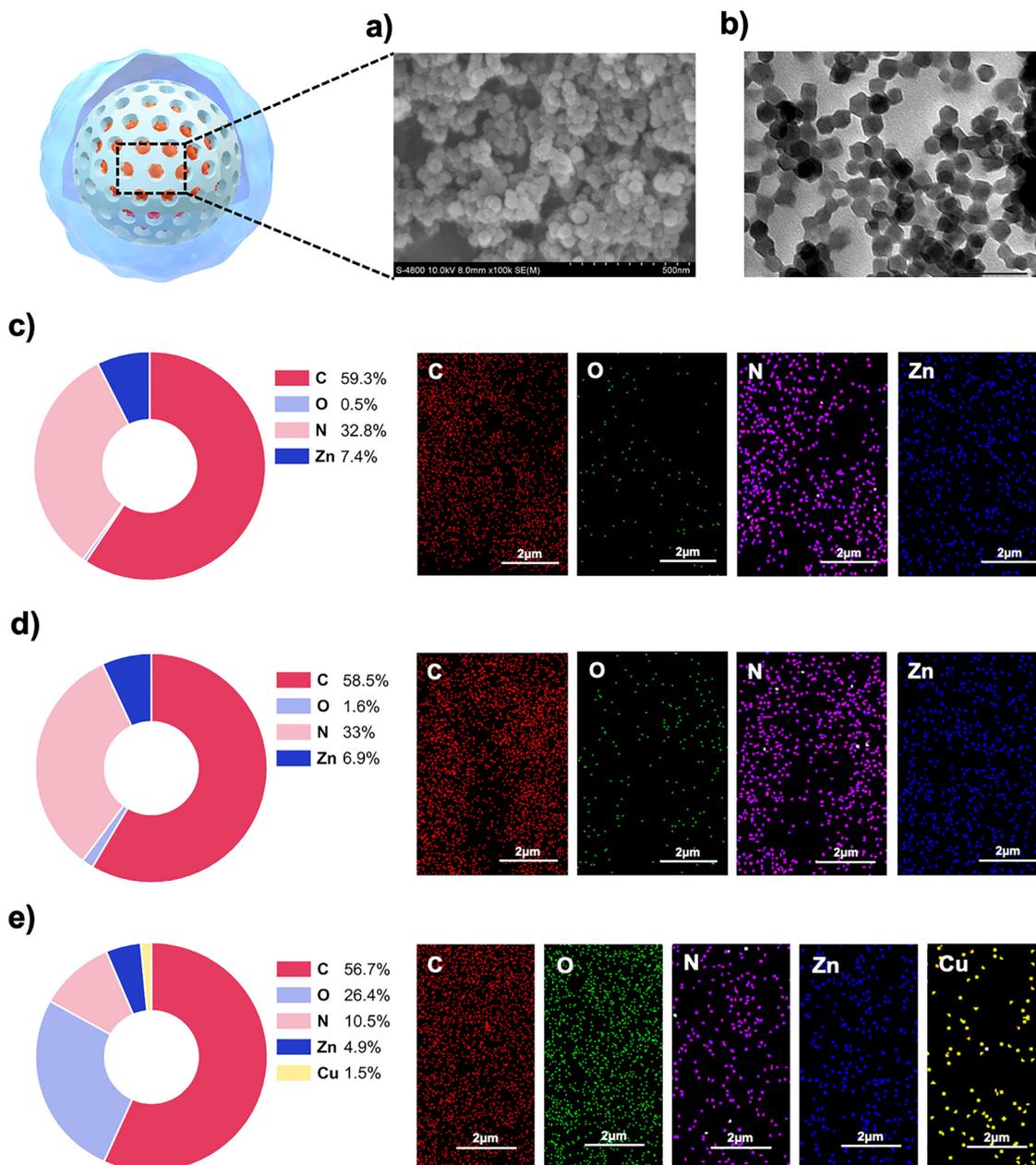

Fig. 3 (a) and (b) Surface morphology of CGCZ examined by (a) FESEM with a scale bar of 500 nm, and (b) TEM with a scale bar of 100 nm. (c)–(e) Elemental analysis of (c) Z, (d) CZ, and (e) CGCZ by EDX, presented as elemental percentages (atomic percentage) along with corresponding EDX mapping, scale bar 2 μm.

CZ shows a lower zeta potential of 20.83 mV, which may be attributed to the partial neutralization of the positive surface charge by negatively charged functional groups (such as hydroxyl and carbonyl groups) present in the CUR molecules. Notably, after functionalization with the CuGA coating, the zeta potential of CGCZ shifts to a negative value (-17.83 mV). This reversal in surface charge may be associated with the tight coating of carboxylate groups from the CuGA on the CZ surface. Interestingly, previous studies have shown that drug delivery systems with negative surface charges often exhibit advantages

in circulation within the bloodstream, thereby potentially enhancing the efficiency of drug delivery to target tissues.[44,45]

The surface properties of the CGCZ bioMOF-on-MOF structure were further examined using FESEM and TEM imaging, EDX spectra, and EDX elemental mapping. As depicted in Fig. 3a and b, the CGCZ particles exhibited a truncated hexagonal-like shape with a uniform size distribution, consistent with the DLS results previously discussed. Furthermore, the successful development of the CGCZ structure was confirmed by EDX spectra and elemental mapping. Specifically, the
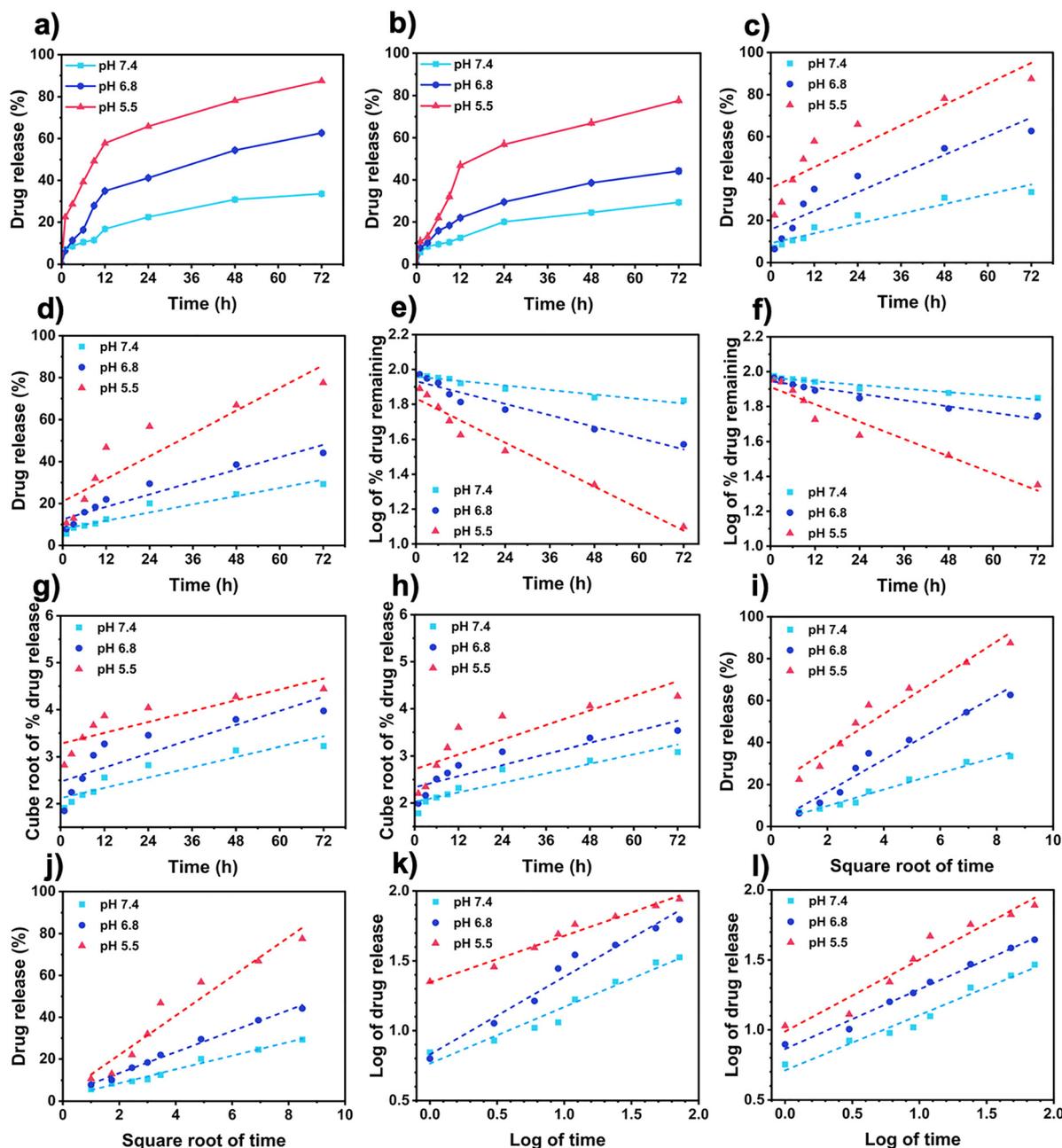

Fig. 4 (a) and (b) pH-Responsive drug release profiles of (a) CZ and (b) CGCZ were evaluated in PBS at pH 7.4, 6.8, and 5.5. The drug release kinetics of (c, e, g, i and k) CZ and (d, f, h, j and l) CGCZ were analyzed using various mathematical models: (c) and (d) zero-order, (e) and (f) first-order, (g) and (h) Hixson–Crowell, (i) and (j) Higuchi, and (k) and (l) Korsmeyer–Peppas models.

Z and CZ samples showed predominant signals of carbon (C), nitrogen (N), and zinc (Zn), along with a minor presence of oxygen (O), which might originate from adsorbed oxygen species on the particle surfaces (Fig. 3c, d and Fig. S3, S4). After the deposition of the CuGA bioMOF coating on CZ, a substantial increase in oxygen content was observed in CGCZ, approximately 16.5 times higher than in CZ (Fig. 3e and Fig. S5). This increase likely arises from the carboxylate groups contributed by the GA ligands of the bioMOF. Additionally, the appearance of a copper (Cu) signal in the EDX spectrum confirmed the successful incorporation of the CuGA coating on the CZ surface. Overall, these results demonstrate that the CGCZ material was successfully developed, with a bioMOF coating formed on the MOF surface as expected.

3.3. Drug release study

To investigate the pH-sensitive drug release behavior of the prepared materials, *in vitro* release studies of CZ and CGCZ were conducted under different pH conditions (7.4, 6.8, and 5.5) using PBS as the release medium at 37 °C. For CZ, the release profile demonstrated a clear pH-dependent trend (Fig. 4a). At pH 7.4, approximately 22.48% of CUR was released after 24 h, increasing slightly to 30.86% after 48 h and stabilizing around 33.59% at 72 h. Under mildly acidic conditions (pH 6.8), CUR release increased significantly, reaching 41.17% at 24 h, 54.41% at 48 h, and 62.69% at 72 h. Notably, at the more acidic pH 5.5, the cumulative release was markedly higher, with 65.82% at 24 h, 78.14% at 48 h, and 87.44% at 72 h. Similarly, CGCZ also exhibited pH-responsive drug release characteristics. At pH 7.4, the release percentages were 20.09% at 24 h, 24.53% at 48 h, and 29.33% at 72 h. At pH 6.8, the release increased to 29.50% at 24 h, 38.59% at 48 h, and 44.21% at 72 h. Under acidic conditions (pH 5.5), the release rate was further enhanced, with 56.78% at 24 h, 66.85% at 48 h, and 77.57% at 72 h (Fig. 4b).

The pH-responsive drug release behavior observed in this study can be attributed to the increased proton concentration (H⁺) in acidic environments, which promotes the cleavage of the coordination bonds between metal ions and organic ligands in both Z MOF and CuGA bioMOF structures. This process facilitates the release of CUR, as illustrated in Fig. 5. These results highlight the potential of both CZ and CGCZ as pH-responsive drug delivery systems, particularly for targeting tumor microenvironments that typically exhibit lower pH values than healthy tissues. Furthermore, when comparing the release profiles of CUR between CZ and CGCZ, it is evident that the presence of the CuGA bioMOF shell on CGCZ effectively controls drug release by acting as a "gatekeeper" providing an additional diffusion barrier and enhancing the structural stability of the material. As a result, CGCZ demonstrates a slower release rate of CUR at all tested pH values compared to CZ. In other words, the CuGA shell not only forms a protective barrier but also helps regulate the release of CUR in various physiological environments.

3.4. Kinetics study

The release kinetics of CUR from CZ and CGCZ at pH 7.4, 6.8, and 5.5 were analyzed using the zero-order, first-order, Hixson–Crowell, Higuchi, and Korsmeyer–Peppas models (Table S1), with the corresponding kinetic plots presented in Fig. 4c–l. For the zero-order model, both CZ and CGCZ exhibited moderate R^2 values (0.797–0.907 for CZ and 0.797–0.927 for CGCZ), suggesting that the release was not perfectly constant over time across all tested pH conditions. The first-order model showed high R^2 values (0.924–0.960 for CZ and 0.926–0.944 for CGCZ), indicating that concentration-dependent release may play a role under these conditions. In contrast, the Hixson–Crowell model displayed lower R^2 values (0.667–0.832 for CZ and 0.660–0.849 for CGCZ), suggesting that erosion or changes in particle geometry had a limited impact on the overall release behavior.
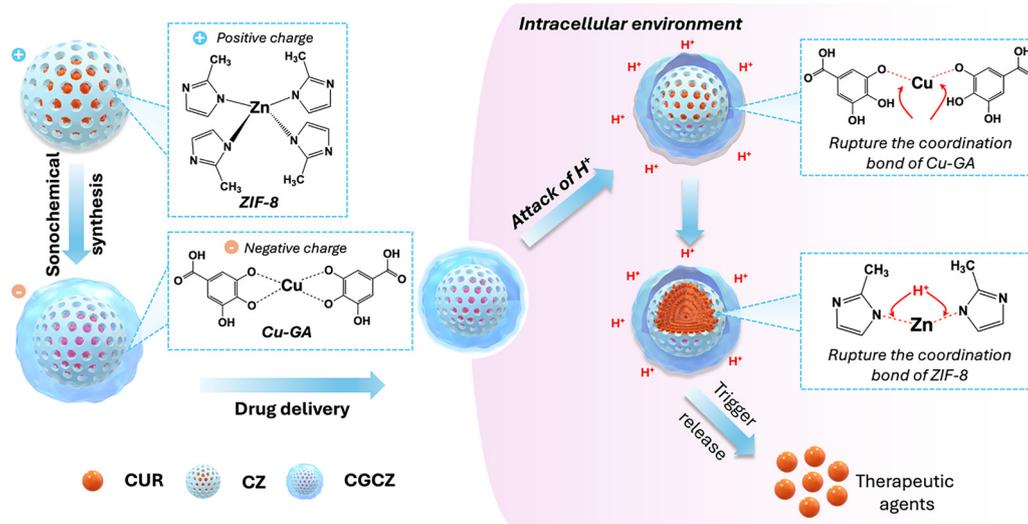

Fig. 5 Illustration of CGCZ synthesis *via* a sonochemical approach and its pH-responsive drug release mechanism. In the acidic intracellular environment, protonation disrupts the coordination bonds of CuGA and Z, thereby triggering the controlled release of therapeutic agents.

The Higuchi model demonstrated a strong fit to the release data, particularly highlighting the diffusion-controlled release behavior. This model fits best for CZ at pH 7.4 ($R^2 = 0.974$) and for CGCZ at both pH 7.4 ($R^2 = 0.982$) and pH 6.8 ($R^2 = 0.989$). Additionally, the Korsmeyer–Peppas model also provided valuable insights into the release mechanism. This model fit well with the release data from CZ at pH 6.8 ($R^2 = 0.958$) and 5.5 ($R^2 = 0.972$), as well as from CGCZ at pH 5.5 ($R^2 = 0.934$). The n values ranged from 0.334 to 0.556 under all pH conditions, indicating that the release process of CUR could be explained by both Fickian diffusion ($n \leq 0.45$) and non-Fickian diffusion ($0.45 < n < 0.89$). Fickian diffusion reflects drug release through the matrix, while non-Fickian diffusion involves a combination of diffusion and relaxation or erosion of the carrier matrix. Overall, these results emphasize that both the Higuchi and Korsmeyer–Peppas models are essential for understanding the CUR release mechanisms from these systems, with diffusion playing a significant role under all tested pH conditions, while polymer relaxation effects become more prominent at lower pH values. Besides, the CuGA coating in CGCZ proved effective in modulating the release profile by providing a pH-responsive diffusion barrier.

3.5. In vitro cytotoxicity study

The cytotoxicity of the Z, CZ, and CGCZ materials was evaluated using the MTT assay on two cell lines: the normal fibroblast cell line L929 and the breast cancer cell line MCF-7, at concentrations ranging from 12.5 to 200 µg mL^{-1} (Fig. 6a–d). The aim was to investigate both the biocompatibility of these materials and their potential selective cytotoxicity toward cancer cells. In the L929 cells, all three samples maintained cell viability above 100% at concentrations from 12.5 to 50 µg mL^{-1}, indicating a high level of safety within this concentration range. At higher concentrations, a dose-dependent increase in cytotoxicity was observed. However, at 200 µg mL^{-1}, CGCZ exhibited the highest biocompatibility compared to Z and CZ, with a viability of 58.63%. This phenomenon can be explained by the negatively charged cell membrane, which promotes strong electrostatic interactions with positively charged particles such as Z and CZ.[46–48] This trend is also in good agreement with previous reports on the biocompatibility of Z and Z-based drug delivery systems on L929 cells.[49–51]

For the MCF-7 cancer cell line, Z showed cell viability ranging from 105.50% at 12.5 µg mL^{-1} to 90.55% at 200 µg mL^{-1}, indicating that Z itself lacked significant anticancer activity. In contrast, CZ demonstrated dose-dependent cytotoxicity toward MCF-7, with cell viability decreasing from 97.81% to 51.26% as the concentration increased. This suggests a moderate anticancer potential, possibly related to the release of CUR from the structure. Importantly, CGCZ exhibited the strongest cytotoxic effect on MCF-7 cells, with viability sharply
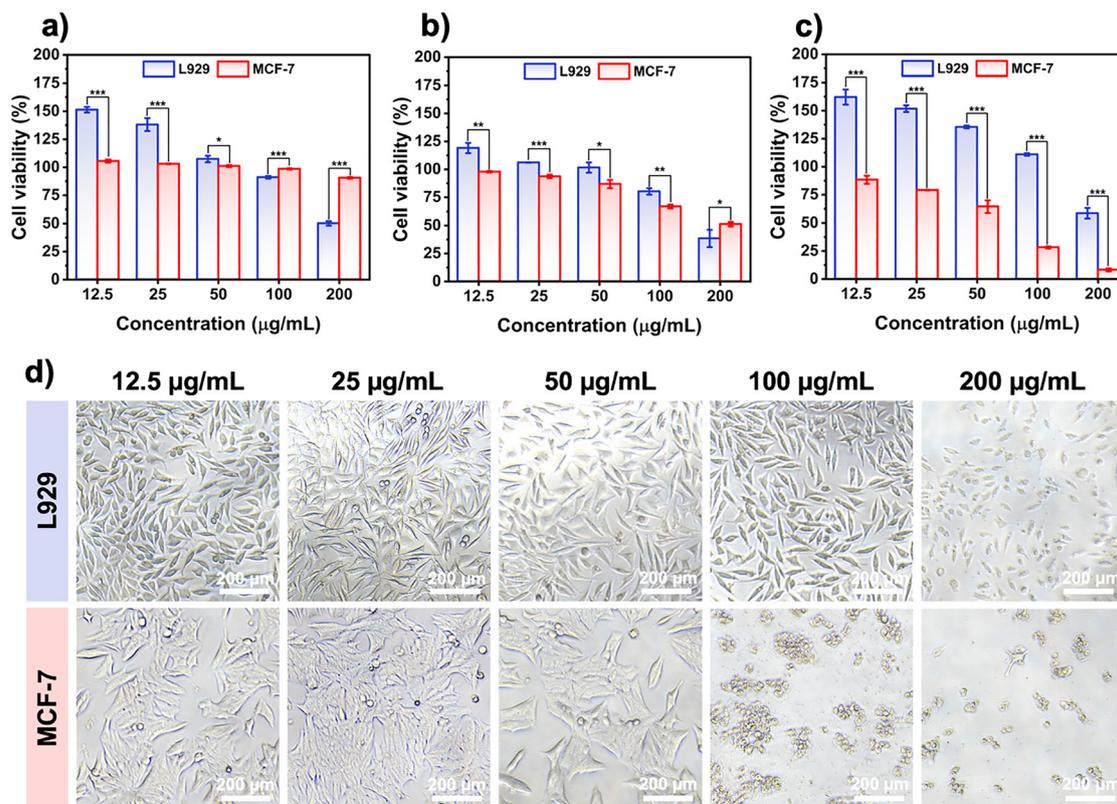

Fig. 6 In vitro cytotoxicity analysis of (a) Z, (b) CZ, and (c) CGCZ formulations against L929 and MCF-7 cell lines, as determined by the MTT assay. (d) Microscopic evaluation of cell morphology in L929 and MCF-7 cells following exposure to CGCZ at varying concentrations (12.5, 25, 50, 100, 200 µg mL^{-1}). Scale bar: 200 µm. Data are presented as mean ± standard deviation, with statistical significance indicated as $p < 0.05$, *$p < 0.01$, and **$p < 0.001$.

decreasing from 88.34% at 12.5 μg mL^{-1} to only 8.19% at 200 μg mL^{-1}. This pronounced activity could be attributed to the synergistic effect between the active compounds CUR and GA within the material structure. Additionally, some studies have suggested that Cu^{2+} ions may react with excess glutathione and hydrogen peroxide in the tumor microenvironment to generate Fenton-like reactions, thereby enhancing the anti-cancer efficacy.[52–54]

Overall, the marked difference in cell viability between L929 and MCF-7 for CGCZ highlights the high selectivity of this material system, likely due to the external CuGA bioMOF coating. This coating enhances the stability of the material in normal cell environments while enabling controlled release of therapeutic agents in the acidic microenvironment of cancer cells. In other words, the CGCZ bioMOF-on-MOF structure was successfully developed and shows potential for controlled drug delivery applications. Nevertheless, as this study primarily focuses on the initial development and evaluation of the material, further *in vitro* and *in vivo* investigations are required. In particular, it will be important to assess the biodegradation pathways of the CGCZ and the potential risk of accumulation in living systems to comprehensively evaluate its efficacy and safety for clinical applications.

4. Conclusion

In summary, the CGCZ bioMOF-on-MOF hybrid nanostructure was successfully synthesized through the direct growth of CuGA bioMOF on the surface of CZ using a sonochemical synthesis method. Notably, this approach aligns with green chemistry principles by utilizing a mild, environmentally friendly synthesis route that reduces the use of hazardous reagents. The physicochemical characterization confirmed that CGCZ inherits favorable properties from its constituents, including a nanoscale dimension of approximately 160 nm, a low PDI (0.19), a high EE (73.60%), and excellent stability maintained over 72 h. Regarding drug release, CGCZ exhibited a pH-dependent and more controlled release profile compared to CZ, with higher release observed at pH 5.5 than at pH 6.8 and 7.4, which could be attributed to the protective bioMOF coating. Kinetic modeling revealed that CGCZ followed the Higuchi model at pH 7.4 (R^2 = 0.982) and pH 6.8 (R^2 = 0.989), while fitting the Korsmeyer–Peppas model at pH 5.5 (R^2 = 0.934). Furthermore, *in vitro* cytotoxicity assays demonstrated that CGCZ exhibited superior selective cytotoxicity compared to Z and CZ. At a concentration of 200 μg mL^{-1}, it maintained over 50% viability of normal L929 cells while effectively killing over 90% of MCF-7 cancer cells. These findings indicate that CGCZ is a promising candidate for controlled drug delivery toward cancer therapy.

Author contributions

Luan Minh Nguyen: conceptualization, methodology, investigation, formal analysis, writing – original draft, writing – review & editing, project administration. Giao Thuy Quynh Vu: investigation, methodology, data curation, formal analysis, visualization. Manh Hoang Tran: methodology, data curation. Thi My Huyen Nguyen: data curation, investigation. Tan Phat Nguyen: methodology, investigation. Qui Thanh Hoai Ta: methodology, investigation. Dieu Linh Tran: methodology, validation, investigation. Dai Hai Nguyen: supervision, investigation, data curation, validation, funding acquisition, project administration.

Conflicts of interest

There are no conflicts to declare.

Data availability

The data supporting this article have been included as part of the SI. See DOI: **https://doi.org/10.1039/d5ma00645g**.

Acknowledgements

References

1 Y. Zhao, J. Cheng, Z. Li, J. Wang and X. Chen, *Adv. Healthcare Mater.*, 2025, **14**, 2402066.

2 R. Perveen, S. Bibi, M. A. Salem, M. H. Helal, A. Afzal, M. A. Wattoo and A. U. Rehman, *J. Mater. Chem. B*, 2025, **13**, 6949–6989.

3 K. M. L. Taylor-Pashow, J. Della Rocca, Z. Xie, S. Tran and W. Lin, *J. Am. Chem. Soc.*, 2009, **131**, 14261–14263.

4 P. Horcajada, C. Serre, M. Vallet-Regí, M. Sebban, F. Taulelle and G. Férey, *Angew. Chem., Int. Ed.*, 2006, **45**, 5974–5978.

5 L. M. Nguyen, Y. Wang, G. T. Quynh Vu, Q. T. Hoai Ta, D. L. Tran, N. H. Nguyen, T. Van Tran, C. Zhang and D. H. Nguyen, *Nanoscale Adv.*, 2025, **7**, 5479–5500.

6 W. Gao, X. Han, L. Li, Y. Xu, M. Xu, Z. Gao and C. Wang, *J. Mater. Chem. B*, 2025, **13**, 3758–3785.

7 Y. Wang, J. Yan, N. Wen, H. Xiong, S. Cai, Q. He, Y. Hu, D. Peng, Z. Liu and Y. Liu, *Biomaterials*, 2020, **230**, 119619.

8 Z. Yu, M. Lepoitevin and C. Serre, *Adv. Healthcare Mater.*, 2025, **14**, 2402630.

9 X. Wang, N. Gao, J. Zhao, G. Ling and P. Zhang, *Coord. Chem. Rev.*, 2024, **517**, 216040.

10 N. Yang, L. Wei, Y. Teng, P. Yu, C. Xiang and J. Liu, *Eur. J. Med. Chem.*, 2024, **274**, 116546.

11 K. Huang, W. Liu, W. Wei, Y. Zhao, P. Zhuang, X. Wang, Y. Wang, Y. Hu and H. Dai, *ACS Nano*, 2022, **16**, 19491–19508.

12 J. He, J. Wu, J. Zheng, Y. Xu, K. Li, S. Yin, Y. Liu, Y. Hu, C. Xie, L. Cai, Y. Du and X. Lu, *ACS Appl. Mater. Interfaces*, 2025, **17**, 11898–11910.

13 A. C. McKinlay, R. E. Morris, P. Horcajada, G. Férey, R. Gref, P. Couvreur and C. Serre, *Angew. Chem., Int. Ed.*, 2010, **49**, 6260–6266.

14 N. Tyagi, Y. H. Wijesundara, J. J. Gassensmith and A. Popat, *Nat. Rev. Mater.*, 2023, **8**, 701–703.

15 M. Koshy, M. Spiotto, L. E. Feldman, J. J. Luke, G. F. Fleming, D. Olson, J. W. Moroney, R. Nanda, A. Rosenberg, A. T. Pearson, A. Juloori, F. Weinberg, C. Ray, R. C. Gaba, P. J. Chang, L. A. Janisch, Z.-Q. Xu, W. Lin, R. R. Weichselbaum and S. J. Chmura, *J. Clin. Oncol.*, 2023, **41**, 2527.

16 Y. Zhong, X. Mu and U. K. Cheang, *Nanoscale Adv.*, 2022, **4**, 1431–1444.

17 Y. Yang, Z. Wang, N. Wang, F. Yan, Z. Shi and S. Feng, *Acta Biomater.*, 2025, **200**, 653–666.

18 Y. Dong, J. Si, J. Feng, T. Xu, X. Xiao, Y. Ji, R. Zhang, X. Sun and Y. Zhu, *Colloids Surf., B*, 2025, **253**, 114712.

19 W. Ni, L. Zhang, H. Zhang, C. Zhang, K. Jiang and X. Cao, *Inorg. Chem.*, 2022, **61**, 3281–3287.

20 A. Maleki, M.-A. Shahbazi, V. Alinezhad and H. A. Santos, *Adv. Healthcare Mater.*, 2020, **9**, 2000248.

21 G. Yang, R. Fan, J. Yang, L. Yi, S. Chen and W. Wan, *Biomaterials*, 2023, **302**, 122347.

22 L. Lin, Q. Li, Y. Yang, C. Zhang, W. Wang, F. Ni and X. Wang, *Acta Biomater.*, 2025, **196**, 380–398.

23 H. Hamedi, S. Javanbakht and R. Mohammadi, *J. Ind. Eng. Chem.*, 2024, **133**, 454–463.

24 Z. Wei, C. Jiang, J. Wang and Y. Chen, *RSC Adv.*, 2024, **14**, 9996–10003.

25 F. B. Ilhami, S. E. Cahyaningrum, A. P. Wardana, N. S. Gultom, H. Subekti, A. Rahmawati and S. Puspitarini, *RSC Adv.*, 2025, **15**, 223–230.

26 L. M. Nguyen, G. T.-Q. Vu, T.-K.-C. Huynh, Q. T. H. Ta, N. H. Nguyen, D. L. Tran and D. H. Nguyen, *Colloids Surf., A*, 2025, **711**, 136321.

27 S. F. Khalilian, M. Tohidi and B. Rastegari, *ACS Omega*, 2023, **8**, 3245–3257.

28 S. Jung, S. Chang, N.-E. Kim, S.-O. Choi, Y.-J. Song, Y. Yuan and J. Kim, *ACS Appl. Nano Mater.*, 2022, **5**, 13671–13679.

29 M. Rahman, M. Kabir, T. Islam, Y. Wang, Q. Meng, H. Liu, S. Chen and S. Wu, *ACS Omega*, 2025, **10**, 3067–3079.

30 X. Wang, G. Fan, Q. Guan, L. Zhao, F. Sun, H. Yang, J. Zhao, J. Zhang, H. Wang, W. Zhang and J. Ma, *ACS Appl. Nano Mater.*, 2022, **5**, 16094–16107.

31 X. Wang, L. Zhou, Y. Shi, W. Wang, P. Li, R. Cui, Y. Wu, F. Wang and Q. Du, *Eur. J. Pharm. Biopharm.*, 2025, **214**, 114773.

32 B. Azhar, A. E. Angkawijaya, S. P. Santoso, C. Gunarto, A. Ayucitra, A. W. Go, P. L. Tran-Nguyen, S. Ismadji and Y.-H. Ju, *Sci. Rep.*, 2020, **10**, 19212.

33 S. Sharma, D. Mittal, A. K. Verma and I. Roy, *ACS Appl. Bio Mater.*, 2019, **2**, 2092–2101.

34 U. Jamil, A. Husain Khoja, R. Liaquat, S. Raza Naqvi, W. Nor Nadyaini Wan Omar and N. Aishah Saidina Amin, *Energy Convers. Manage.*, 2020, **215**, 112934.

35 M. Sharma and P. Kumar, *Inorg. Chem. Commun.*, 2025, **171**, 113590.

36 Nugraha, N. Hanifah, A. Muslihati, M. F. Raihan, N. L. Wulan Septiani and B. Yuliarto, *RSC Adv.*, 2025, **15**, 7897–7904.

37 G. T.-Q. Vu, L. M. Nguyen, K. N. Nguyen Do, D. L. Tran, T. Van Vo, D. H. Nguyen and L. B. Vong, *ACS Appl. Bio Mater.*, 2025, **8**, 2052–2064.

38 H. Hamedi, S. Javanbakht and R. Mohammadi, *J. Ind. Eng. Chem.*, 2024, **133**, 454–463.

39 O. G. Hussein, Y. Mohamed, N. Mostafa and A. M. Mahmoud, *RSC Adv.*, 2025, **15**, 11730–11738.

40 S. Elmehrath, K. Ahsan, N. Munawar, A. Alzamly, H. L. Nguyen and Y. Greish, *RSC Adv.*, 2024, **14**, 15821–15831.

41 P. Nezhad-Mokhtari, H. Hamishehkar, M. R. Farahpour, A. Mehdipour, R. Rahbarghazi, M. Milani and M. Mehrali, *Chem. Eng. J.*, 2024, **489**, 150992.

42 M. Taheri, D. Ashok, T. Sen, T. G. Enge, N. K. Verma, A. Tricoli, A. Lowe, D. R. Nisbet and T. Tsuzuki, *Chem. Eng. J.*, 2021, **413**, 127511.

43 S. Yamane, A. H. Bin Yusri, P. Chen, A. J. van der Vlies, A. Ben Mabrouk, I. Fetzer and U. Hasegawa, *Macromol. Biosci.*, 2025, **25**, 2400382.

44 Md. L. Amin, J. Y. Joo, D. K. Yi and S. S. A. An, *J. Controlled Release*, 2015, **207**, 131–142.

45 B. Chertok, A. E. David and V. C. Yang, *Biomaterials*, 2010, **31**, 6317–6324.

46 M. Weiss, J. Fan, M. Claudel, T. Sonntag, P. Didier, C. Ronzani, L. Lebeau and F. Pons, *J. Nanobiotechnol.*, 2021, **19**, 5.

47 S. Balog, M. S. de Almeida, P. Taladriz-Blanco, B. Rothen-Rutishauser and A. Petri-Fink, *Curr. Opin. Biotechnol*, 2024, **87**, 103128.

48 M. Xiong, Y. Zhang, H. Zhang, Q. Shao, Q. Hu, J. Ma, Y. Wan, L. Guo, X. Wan, H. Sun, Z. Yuan and H. Wan, *Adv. Sci.*, 2024, **11**, 2402465.

49 J. Zhang, Y. Xue, L. Zhang, J. Chen, D. Ma, Y. Zhang and Y. Han, *ACS Appl. Mater. Interfaces*, 2025, **17**, 20901–20918.

50 Q. Sun, H. Bi, Z. Wang, C. Li, X. Wang, J. Xu, H. Zhu, R. Zhao, F. He, S. Gai and P. Yang, *Biomaterials*, 2019, **223**, 119473.

51 P. P. N. C. Kumari, H. Asadevi, P. S. Vindhya, V. T. Kavitha, A. S. Nair and R. Raghunandan, *J. Drug Delivery Sci. Technol.*, 2023, **90**, 105147.

52 M. Ji, H. Liu, J. Gou, T. Yin, H. He, Y. Zhang and X. Tang, *Nanoscale*, 2023, **15**, 8948–8971.

53 C. Gong, J. Zhao, X. Meng, Z. Yang and H. Dong, *Chem. Eng. J.*, 2022, **435**, 135083.

54 K. Zhang, X. Meng, Z. Yang, H. Dong and X. Zhang, *Biomaterials*, 2020, **258**, 120278.